Mechanics Modeling of Multisegment Rod-Driven Continuum Robots

William S. Rone
Robotics and Mechatronics Lab,
Department of Mechanical and Aerospace Engineering,
The George Washington University,
801 22nd Street, NW,
Washington, DC 20052

Pinhas Ben-Tzvi
Robotics and Mechatronics Lab,
Department of Mechanical and Aerospace Engineering,
The George Washington University,
801 22nd Street, NW,
Washington, DC 20052
e-mail: bentzvi@gwu.edu

This paper presents a novel modeling approach for the mechanics of multisegment, rod-driven continuum robots. This modeling approach utilizes a high-fidelity lumped parameter model that captures the variation in curvature along the robot while simultaneously defined by a discrete set of variables and utilizes the principle of virtual power to formulate the statics and dynamics of the continuum robot as a set of algebraic equations for the static model and as a set of coupled ordinary differential equations (ODEs) in time for the dynamic model. The actuation loading on the robot by the actuation rods is formulated based on the calculation of contact forces that result in rod equilibrium. Numerical optimization calculates the magnitudes of these forces, and an iterative solver simultaneously estimates the robot's friction and contact forces. In addition, modeling considerations including variable elastic loading among segments and mutual segment loading due to rods terminating at different disks are presented. The resulting static and dynamic models have been compared to dynamic finite element analyses and experimental results to validate their accuracy. [DOI: 10.1115/1.4027235]

Keywords: continuum robotics, method of virtual power, rod-driven mechanics

1 Introduction

Modeling continuum robot mechanics poses several challenges in comparison to conventional robots with discrete joints [1], including: (1) *Joint Space Definition*: there is no intrinsic discrete set of variables that composes the joint space—the arm's continuum nature leads to theoretically infinite degrees of freedom; (2) *Importance of Elasticity*: unlike most conventional robots in which elasticity is considered as secondary effect, in continuum robots elasticity plays a key role in determining the continuum robot's shape; and (3) *Actuation Localization*: continuum robots typically localize actuation at the base of arm and transmit the actuation along the structure, and this actuation transmission to a distal segment will also load proximal segments through which it is routed.

In addition, there are a wide variety of continuum robotic structures presented in the literature. The most common are cable-driven robots [2–5] where a backbone is deformed by cabling along the robot's length and terminating at different segments. Rod-driven robots [6,7] use elastic rods instead of cabling, enabling transmission of compressive forces and increasing the structure's rigidity. Pneumatic and hydraulic continuum robots [8–11] utilize segments composed of pneumatic or hydraulic "muscles" to bend into desired shapes. Concentric-tube robots [12,13] are composed of concentric precurved elastic tubes, with the relative displacement and orientation controlling the robot's shape. Shape memory alloy spring pairs have also been used to actuate an octopus-like continuum robot [14].

This research is motivated by the need for high fidelity models of continuum robots defined by a set of discrete parameters. Most previous research modeling continuum robot mechanics may be grouped into two categories: low-fidelity lumped parameter models and high-fidelity distributed parameter models. Structurally, continuum robots are composed of a series of actuated segments, as shown in Fig. 1. In low-fidelity lumped parameter models, each segment is represented by a single circular arc, and the robot is defined as the serial chain of these arcs. In the high-fidelity distributed parameter models, the continuum robot is considered as either a one-dimensional generalized spatial curve or a three-dimensional elastic body. Dynamic models have been derived for both approaches to model the robot's time-varying behavior. In addition, kinematic and static models have been formulated for the lumped and distributed parameter time-invariant models.

Existing low-fidelity lumped parameter models do not account for curvature variations along the continuum robot. These variations may be due to external loading (e.g., gravity or external contact) or internal loading (e.g., friction). Webster and Jones [15] provide an exhaustive review of time-invariant constant curvature models. Chirikjian and Burdick [16] studied curve-fitting using Bessel functions to generated a desired configuration from task requirements, then map actuation variables to match the shape. Dynamic time-varying models have included Tatlicioglu et al. [17] and Godage et al. [8] to adapt the Euler–Lagrange equations for pneumatic [17] and hydraulic [8] continuum robots. When only considering elasticity and actuation and with special design considerations for the arm itself (e.g., optimal spacing between disks), this is a valid assumption. However, in the presence of gravity, inertial and other external forces, the accuracy is reduced [18].

Existing high-fidelity distributed parameter models allow an arbitrary robot shape in response to loading, allowing for curvature variations along each segment. Time-invariant models include Cosserat rod and local energy minimization. Jones et al. [18] and Renda et al. [19] used Cosserat rod theory to represent the rod as a one-dimensional curve in space with all relevant elastic, gravitational, and actuation forces modeled as applied loading. Rucker et al. [20] determined equilibrium by tracking the local minimization of an energy function during motion of a concentric tube robot. Dynamic time-varying models include work by Rucker and Webster [21], Spillmann and Teschner [22] and Lang et al. [23] to adapt time-invariant models with the inclusion of inertial effects. Chirikjian [24] approximated a serpentine robot as a continuum body and formulates the dynamics using the continuum mechanics conservation equations. Gravagne et al. [25] utilized Hamilton's principle to calculate the dynamics as a set of partial differential equations for a cable-driven robot.

Contributed by the Mechanisms and Robotics Committee of ASME for publication in the Journal of Mechanisms and Robotics. Manuscript received May 22, 2013; final manuscript received February 20, 2014; published online June 5, 2014. Assoc. Editor: Vijay Kumar.

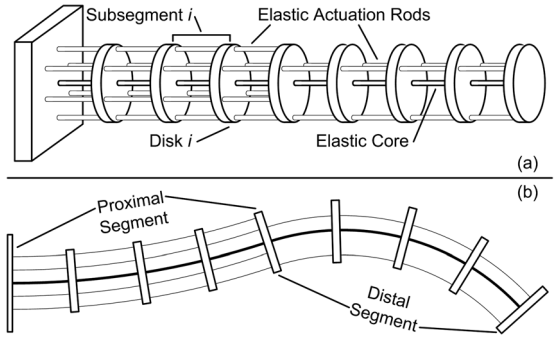

Fig. 1 Multisegment continuum robotic structure (*a*) three-dimensional representation of structure with eight disks rigidly mounted along an elastic core, with six actuation rods to control shape. Three rods terminate at the fourth disk, and three rods terminate at the eighth disk. (*b*) Typical planar mode shape of two-segment manipulator illustrating bending of the proximal and distal segments.

Existing work in high-fidelity lumped parameter models has been limited. Rone and Ben-Tzvi [26,27] utilized a subsegment-based discretization to utilize subsegment curvature and torsional twist angles to define mechanics models using the principles of virtual work [26] and power [27] for a cable-driven continuum robot. Xu and Simaan [28] used a subsegment-based analysis for rod-driven continuum robot statics using constrained minimization. Jung et al. [29] utilized a lumped mass model for each disk and Newton's second law to formulate the dynamic equations of motion for a cable-driven continuum robot. Giri and Walker [30] utilized a similar mass-spring-damper model to simulate a pneumatic-muscle based continuum robot using Lagrangian mechanics.

This high-fidelity lumped parameter model approach provides numerous benefits to a variety of applications in comparison to the low-fidelity lumped parameter models described previously, including the ability to capture variations in curvature in manipulation tasks due to contact forces, such as bending around a corner or wrapping around an object. In dynamic applications, such as the use of a continuum robot as a tail on a legged system, the model could be used to more accurately predict the tail's dynamic forces and moments on the chassis to assist in stabilization and maneuvering. Furthermore, the fidelity of the discretization of each segment may be tuned based on the required level of accuracy in the model. In comparison to the current high-fidelity distributed parameter models, the lumped parameter model is more amenable to rapid, possibly real-time, calculation on currently available hardware. In addition, the virtual power model allows for the generation of dynamic equations of motion for the exact number of parameters used to define the model, unlike [29], and does not require differentiable energy functions for the physical effects, unlike [30].

1.1 Contribution. This paper builds on the authors' previous work in continuum robot mechanics [26,27] by considering rod-driven continuum robot actuation structures and multisegment continuum robots. For the rod-driven actuation structure, the calculation of contact forces between the rod and disks is significantly more complicated than between cables and disks. As a result, this paper focuses more on the derivation and calculations associated with this feature, as compared to the focus in Ref. [27] on the overarching virtual power model. For multisegment continuum robots, this paper presents the modifications to the single segment model required to account for actuation rods terminating at disks other than the final disk. The virtual power formulation makes this a relatively straightforward extension, though calculation of the inertial, elastic, gravitational and actuation loading will all be impacted.

1.2 Outline. This paper is organized as follows: Sec. 2 provides background into the method of virtual power and the rod-driven robot structure considered in this work. Section 3 presents the continuum robot kinematic analysis, including formulations for the disk positions, velocities, and accelerations. Section 4 derives the rod-driven continuum robot mechanics model, with particular emphasis on elasticity and actuation. Section 5 describes the generalization of single-segment modeling to a multisegment structure. Section 6 describes the model's numerical implementation and compares the results to dynamic finite element analysis (FEA) and experimental results. Section 7 summarizes the paper and describes future work.

2 Background

In this section, the theoretical background for the method of virtual power is provided, along with a description of the rod-driven continuum robot structure.

2.1 Principle of Virtual Power. The principle of virtual power, also called Kane's method, uses variational calculus to calculate mechanics by finding the stationary point of the virtual power of the external forces and moments applied to the system [31] and has been previously applied to both rigid-link [32,33] and flexible [34] robots. This virtual power P is found using Eq. (1), where $\boldsymbol{M}_{i,\text{ex}}$ and $\boldsymbol{F}_{i,\text{ex}}$ are the net external moment and force on rigid body i and $\boldsymbol{\omega}_i$ and $\boldsymbol{v}_i$ are the angular and linear velocity at the body i center-of-mass.

$$P = \sum_i \left(\boldsymbol{M}_{i,\text{ex}} \cdot \boldsymbol{\omega}_i + \boldsymbol{F}_{i,\text{ex}} \cdot \boldsymbol{v}_i\right) \tag{1}$$

To take the variation, the generalized coordinates q_k and velocities $\dot{q}_k$ are chosen to define the system's dynamic configuration. Each body's velocities may be defined with respect to $\dot{q}_k$ using the partial angular velocity $\boldsymbol{\omega}_{i,k}$ and the partial linear velocity $\boldsymbol{v}_{i,k}$, shown in Eq. (2). Using this formulation, the virtual power variation ΔP in Eq. (3) may be found. To calculate the equilibrium, set $\Delta P = 0$. For this to be true for any arbitrary variation in $\dot{q}_k$, Eq. (4) must be true, providing the mechanics governing equations.

$$\boldsymbol{\omega}_i = \boldsymbol{\omega}_{i,k}\dot{q}_k, \quad \boldsymbol{v}_i = \boldsymbol{v}_{i,k}\dot{q}_k \tag{2}$$

$$\Delta P = \left[\sum_i \left(\boldsymbol{M}_{i,\text{ex}} \cdot \boldsymbol{\omega}_{i,k} + \boldsymbol{F}_{i,\text{ex}} \cdot \boldsymbol{v}_{i,k}\right)\right] \Delta\dot{q}_k \tag{3}$$

$$\sum_i \left(\boldsymbol{M}_{i,\text{ex}} \cdot \boldsymbol{\omega}_{i,k} + \boldsymbol{F}_{i,\text{ex}} \cdot \boldsymbol{v}_{i,k}\right) = 0 \tag{4}$$

Equation (5) defines the terms that will contributed to $\boldsymbol{M}_{i,\text{ex}}$ and $\boldsymbol{F}_{i,\text{ex}}$ in this paper: the inertial effects force $\boldsymbol{F}_{i,\text{inr}}$ and moment $\boldsymbol{M}_{i,\text{inr}}$, the elastic effects moment $\boldsymbol{M}_{i,\text{el}}$, the gravitational effects force $\boldsymbol{F}_{i,\text{gr}}$ and the actuation effects (with or without friction) force $\boldsymbol{F}_{i,\text{act}}$ and moment $\boldsymbol{M}_{i,\text{act}}$. A key benefit of virtual power is its ability to directly include forces and moments in the mechanics calculation without requiring the calculation of internal forces between bodies. Section 4 provides the analysis for the calculation of the forces and moments that make up $\boldsymbol{M}_{i,\text{ex}}$ and $\boldsymbol{F}_{i,\text{ex}}$.

$$\begin{aligned} \boldsymbol{M}_{i,\text{ex}} &= \boldsymbol{M}_{i,\text{inr}} + \boldsymbol{M}_{i,\text{el}} + \boldsymbol{M}_{i,\text{act}}, \\ \boldsymbol{F}_{i,\text{ex}} &= \boldsymbol{F}_{i,\text{inr}} + \boldsymbol{F}_{i,\text{gr}} + \boldsymbol{F}_{i,\text{act}} \end{aligned} \tag{5}$$

2.2 Rod-Driven Continuum Robotic Structure. Figure 1 shows the rod-driven structure under consideration. It is composed of eight disks rigidly mounted along an elastic core. Six rods actuate the structure, with three terminating at the fourth and eighth disks, resulting in a two-segment structure.

This structure leads to a natural choice for the robot's discretization, shown in Fig. 2. The mass and inertia of the core and rods

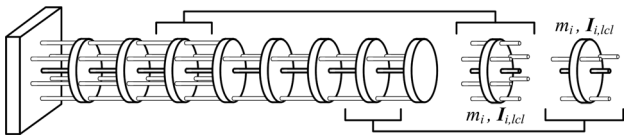

Fig. 2 Discretization of proximal and distal subsegments accounting for the disk, core, and rods, with mass m_i and moment of inertia $I_{i,\mathrm{lcl}}$

surrounding each disk are added to the mass and inertia of that disk, resulting in a generalized rigid-body. For simplicity, the generalized rigid-bodies composing the continuum robot will continue to be referred to as disks. The kinematics assumes circular subsegment arcs separate each disk. Based on the core and rod properties, each subsegment's bending applies moments to the subsegment's two adjacent disks. Compressive and shear loads are neglected due to the core's relative incompressibility compared to its bending. Torsion is neglected in this paper to simplify the initial analysis. Without torsion, the actuation rod bending is assumed to be coplanar with the elastic core, enabling calculation based on elastic core bending. In addition, torsion would also impact the calculation of contact forces along the continuum robot. As discussed in Sec. 7, modeling torsion is a key aspect of the future work.

3 Kinematic Analysis

In this section, the continuum robot kinematics are derived, including the local disk linear positions and angular velocities, and the global positions, velocities and accelerations of the disks.

3.1 Local Coordinates, Linear Position, and Angular Velocity. As discussed in Sec. 2.1, the generalized coordinates and velocities define the robot's dynamic configuration. Figure 3 illustrates the model's generalized coordinates, as well as other calculated values. Based on the subsegment discretization in Sec. 2.2, two coordinates define the difference in position and orientation between two adjacent disks: the orthogonal subsegment curvatures β_i (x-z plane) and γ_i (y-z plane). The vector $\boldsymbol{q}_{i,\mathrm{lcl}}$ in Eq. (6) of these variables defines the generalized coordinates for subsegment i, and the collection of these vectors for an n-subsegment continuum robot results in the robot's generalized coordinates q_k, shown in Eq. (7).

$$\boldsymbol{q}_{i,\mathrm{lcl}} = \begin{bmatrix} \beta_i, & \gamma_i \end{bmatrix}^T \tag{6}$$

$$q_k = \begin{bmatrix} \boldsymbol{q}_{1,\mathrm{lcl}}^T, & \boldsymbol{q}_{2,\mathrm{lcl}}^T, & \cdots, & \boldsymbol{q}_{n,\mathrm{lcl}}^T \end{bmatrix}^T \tag{7}$$

To simplify the analysis, three intermediate variables are defined in Eq. (8): the subsegment curvature magnitude k_i, the bending plane angle φ_i and the subsegment bending angle θ_i, where L_0 is the spacing between disks. The atan2 function is a four quadrant mapping of the two quadrant atan(γ_i/β_i) function.

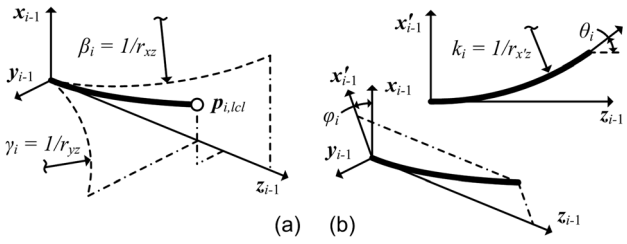

Fig. 3 (*a*) Illustration of the *x*-*z* plane curvature β_i and the *y*-*z* plane curvature γ_i. (*b*) Illustration of the intermediate coordinates: the in-plane curvature k_i, the bending plane angle φ_i, and the subsegment bending angle θ_i.

$$k_i = \sqrt{\beta_i^2 + \gamma_i^2}, \quad \varphi_i = \mathrm{atan2}(\gamma_i, \beta_i), \quad \theta_i = k_i L_0 \tag{8}$$

Each disk has a coordinate system coincident with its center-of-mass. For disk i, the local coordinate system is $\boldsymbol{x}_i\, \boldsymbol{y}_i\, \boldsymbol{z}_i$. The robot's base global frame is $\boldsymbol{x}_0\, \boldsymbol{y}_0\, \boldsymbol{z}_0$.

Based on geometric analysis [15], the local position vector $\boldsymbol{p}_{i,\mathrm{lcl}}$ of the disk i center-of-mass relative to the frame $i-1$ is calculated in Eq. (9). For this and following expressions, the limit $\lim_{k\to 0}$ is substituted for the given expression when $k_i = 0$.

$$\boldsymbol{p}_{i,\mathrm{lcl}} = \begin{bmatrix} c_{\varphi_i}(1 - c_{\theta_i})/k_i, & s_{\varphi_i}(1 - c_{\theta_i})/k_i, & s_{\theta_i}/k_i \end{bmatrix}^T \tag{9}$$

To define the orientation, the unit vectors of the frame i in frame $i-1$ are used. Three sequential rotations define the rotation matrix: (1) rotating θ_i around the $\boldsymbol{y}_{i-1}$ axis, (2) rotating φ_i around the $\boldsymbol{z}_{i-1}$ axis, and (3) rotating $-\varphi_i$ around the current $\boldsymbol{z}_i$ axis. The third rotation ensures the frame is not subjected to a "torsional" rotation along the subsegment [15]. The resulting rotation matrix $\boldsymbol{R}_{i,\mathrm{lcl}}$ is shown in Eq. (10). The columns of $\boldsymbol{R}_{i,\mathrm{lcl}}$ correspond to the tangent vector $\boldsymbol{t}_{i,\mathrm{lcl}}$, the normal vector $\boldsymbol{n}_{i,\mathrm{lcl}}$ and binormal vector $\boldsymbol{b}_{i,\mathrm{lcl}}$, shown in Eq. (11).

$$\boldsymbol{R}_{i,\mathrm{lcl}} = \begin{bmatrix} c_{\varphi_i}^2(c_{\theta_i} - 1) + 1 & s_{\varphi_i} c_{\varphi_i}(c_{\theta_i} - 1) & c_{\varphi_i} c_{\theta_i} \\ s_{\varphi_i} c_{\varphi_i}(c_{\theta_i} - 1) & c_{\varphi_i}^2(1 - c_{\theta_i}) + c_{\theta_i} & s_{\varphi_i} c_{\theta_i} \\ -c_{\varphi_i} s_{\theta_i} & -s_{\varphi_i} s_{\theta_i} & s_{\theta_i} \end{bmatrix} \tag{10}$$

$$\begin{bmatrix} \boldsymbol{n}_{i,\mathrm{lcl}}, & \boldsymbol{b}_{i,\mathrm{lcl}}, & \boldsymbol{t}_{i,\mathrm{lcl}} \end{bmatrix} = \boldsymbol{R}_{i,\mathrm{lcl}} \tag{11}$$

The local angular velocity $\boldsymbol{\omega}_{i,\mathrm{lcl}}$ is defined based on the "motion" of $\boldsymbol{t}_{i,\mathrm{lcl}}$. It is known that $\dot{\boldsymbol{t}}_{i,\mathrm{lcl}} = \boldsymbol{\omega}_{i,\mathrm{lcl}} \times \boldsymbol{t}_{i,\mathrm{lcl}}$ and $0 = \boldsymbol{\omega}_{i,\mathrm{lcl}} \cdot \boldsymbol{t}_{i,\mathrm{lcl}}$ (because torsion is neglected). With these properties, $\boldsymbol{\omega}_{i,\mathrm{lcl}}$ is found by simplifying the cross product of $\boldsymbol{t}_{i,\mathrm{lcl}}$ and $\boldsymbol{\omega}_{i,\mathrm{lcl}} \times \boldsymbol{t}_{i,\mathrm{lcl}}$, shown in below equation:

$$\begin{aligned} \boldsymbol{t}_{i,\mathrm{lcl}} \times (\boldsymbol{\omega}_{i,\mathrm{lcl}} \times \boldsymbol{t}_{i,\mathrm{lcl}}) &= (\boldsymbol{t}_{i,\mathrm{lcl}} \cdot \boldsymbol{t}_{i,\mathrm{lcl}})\boldsymbol{\omega}_{i,\mathrm{lcl}} - (\boldsymbol{\omega}_{i,\mathrm{lcl}} \cdot \boldsymbol{t}_{i,\mathrm{lcl}})\boldsymbol{t}_{i,\mathrm{lcl}} \\ \boldsymbol{\omega}_{i,\mathrm{lcl}} &= \boldsymbol{t}_{i,\mathrm{lcl}} \times \dot{\boldsymbol{t}}_{i,\mathrm{lcl}} \end{aligned} \tag{12}$$

3.2 Global Positions, Velocities, and Accelerations. Rotation matrices $\boldsymbol{R}_i$ for each disk's orientation may be found recursively, shown in Eq. (13), and the three global unit vectors that define this frame are denoted $\boldsymbol{x}_i$, $\boldsymbol{y}_i$, and $\boldsymbol{z}_i$ and are defined in Eq. (14). Using these rotations, the disk i positions $\boldsymbol{p}_i$ and angular velocities $\boldsymbol{\omega}_i$ are found recursively, shown in Eqs. (15) and (16).

$$\boldsymbol{R}_i = \begin{cases} \boldsymbol{R}_{i,\mathrm{lcl}} & i = 1 \\ \boldsymbol{R}_{i-1}\boldsymbol{R}_{i,\mathrm{lcl}} & i > 1 \end{cases} \tag{13}$$

$$\begin{bmatrix} \boldsymbol{x}_i, & \boldsymbol{y}_i, & \boldsymbol{z}_i \end{bmatrix} = \boldsymbol{R}_i \tag{14}$$

$$\boldsymbol{p}_i = \begin{cases} \boldsymbol{p}_{i,\mathrm{lcl}} & i = 1 \\ \boldsymbol{p}_{i-1} + \boldsymbol{R}_{i-1}\boldsymbol{p}_{i,\mathrm{lcl}} & i > 1 \end{cases} \tag{15}$$

$$\boldsymbol{\omega}_i = \begin{cases} \boldsymbol{\omega}_{i,\mathrm{lcl}} & i = 1 \\ \boldsymbol{\omega}_{i-1} + \boldsymbol{R}_{i-1}\boldsymbol{\omega}_{i,\mathrm{lcl}} & i > 1 \end{cases} \tag{16}$$

To simplify the following analyses, note that $\dot{\boldsymbol{R}}_i = \boldsymbol{\omega}_i \times \boldsymbol{R}_i$. The linear velocities $\boldsymbol{v}_i$ and angular accelerations $\boldsymbol{\alpha}_i$ are found from the derivatives of Eqs. (15) and (16), shown in Eqs. (17) and (18). The linear accelerations $\boldsymbol{a}_i$ are found from the derivative of Eq. (17), shown in Eq. (19).

$$\boldsymbol{v}_i = \begin{cases} \dot{\boldsymbol{p}}_{i,\mathrm{lcl}} & i = 1 \\ \boldsymbol{v}_{i-1} + \boldsymbol{\omega}_{i-1} \times \boldsymbol{R}_{i-1} p_{i,\mathrm{lcl}} + \boldsymbol{R}_{i-1}\dot{\boldsymbol{p}}_{i,\mathrm{lcl}} & i > 1 \end{cases} \tag{17}$$

$$\boldsymbol{\alpha}_i = \begin{cases} \dot{\boldsymbol{\omega}}_{i,\mathrm{lcl}} & i = 1 \\ \boldsymbol{\alpha}_{i-1} + \boldsymbol{\omega}_{i-1} \times \boldsymbol{R}_{i-1}\boldsymbol{\omega}_{i,\mathrm{lcl}} + \boldsymbol{R}_{i-1}\dot{\boldsymbol{\omega}}_{i,\mathrm{lcl}} & i > 1 \end{cases} \tag{18}$$

$$\boldsymbol{a}_i = \begin{cases} \ddot{\boldsymbol{p}}_{i,\mathrm{lcl}} & i = 1 \\ \begin{pmatrix} \boldsymbol{a}_{i-1} + \dot{\boldsymbol{\omega}}_{i-1} \times \boldsymbol{R}_{i-1}\boldsymbol{p}_{i,\mathrm{lcl}} + 2\boldsymbol{\omega}_{i-1} \times \boldsymbol{R}_{i-1}\dot{\boldsymbol{p}}_{i,\mathrm{lcl}} \\ + \boldsymbol{\omega}_{i-1} \times \left(\boldsymbol{\omega}_{i-1} \times \boldsymbol{R}_{i-1}\boldsymbol{p}_{i,\mathrm{lcl}}\right) + \boldsymbol{R}_{i-1}\ddot{\boldsymbol{p}}_{i,\mathrm{lcl}} \end{pmatrix} & i > 1 \end{cases} \tag{19}$$

4 Rod-Driven Mechanics

In this section, the components of $\boldsymbol{M}_{i,\mathrm{ex}}$ and $\boldsymbol{F}_{i,\mathrm{ex}}$ from Eq. (5) are formulated for the rod-driven continuum robot structure. A single-segment, three actuation rod continuum robot is used for the analysis in this section. This analysis will be generalized for a multisegment structure in Sec. 5.

4.1 Inertial Effects. Equations (20) and (21) define the $\boldsymbol{F}_{i,\mathrm{inr}}$ and $\boldsymbol{M}_{i,\mathrm{inr}}$, where m_i is the disk's mass and $\boldsymbol{I}_i$ is the disk's moment of inertia. $\boldsymbol{I}_i$ depends on the disk's orientation and the local radial ($I_{i,xx,\mathrm{lcl}}$ and $I_{i,yy,\mathrm{lcl}}$) and axial ($I_{i,zz,\mathrm{lcl}}$) moments of inertia, shown in Eq. (22).

$$\boldsymbol{F}_{i,\mathrm{inr}} = -m_i\boldsymbol{a}_i \tag{20}$$

$$\boldsymbol{M}_{i,\mathrm{inr}} = -\boldsymbol{I}_i\boldsymbol{\alpha}_i - \boldsymbol{\omega}_i \times \boldsymbol{I}_i\boldsymbol{\omega}_i \tag{21}$$

$$\boldsymbol{I}_i = \boldsymbol{R}_i\boldsymbol{I}_{i,\mathrm{lcl}}\boldsymbol{R}_i^T, \quad \boldsymbol{I}_{i,\mathrm{lcl}} = \begin{bmatrix} I_{i,xx,\mathrm{lcl}} & 0 & 0 \\ 0 & I_{i,yy,\mathrm{lcl}} & 0 \\ 0 & 0 & I_{i,zz,\mathrm{lcl}} \end{bmatrix} \tag{22}$$

4.2 Elastic Effects. Elastic effects account for the forces and moments generated by the robot in response to deformation. For the rod-driven continuum robot structure, the continuum core and actuation rods are sources of elasticity. The elastic effects for both are assumed to be purely bending, as discussed in Sec. 2.2.

The continuum core bending moment magnitude $M_{i,\mathrm{bnd},c}$ is defined in Eq. (23), where E_c is the core's Young's modulus and $J_{xx,c}$ is the core cross section's second moment of area.

$$M_{i,\mathrm{bnd},c} = E_c J_{xx,c} k_i \tag{23}$$

Each subsegment's three or six actuation rods are assumed to bend as circular arcs in planes parallel to the core subsegment bending defined by k_i and φ_i. The curvature $k_{i,j}$ of the jth rod in the ith subsegment is calculated from k_i, φ_i and the local routing hole position $\boldsymbol{r}_{j,\mathrm{hl,lcl}}$. The rod subsegment curvatures are calculated by assuming the actuation rods' circular arcs are concentric with the core's circular arc. This assumption is valid because the core and each rod are assumed to be held tangent to the two surrounding disks. The intersection of the two disk planes is the core and rod arc's center.

The rod curvatures are found by determining the radius of curvature offset $\delta_{i,j}$ of the rod relative to the core's radius of curvature $1/k_{i,j}$, defined in Eq. (24) where r_h is distance between the hole and disk center. Figure 4 illustrates the hole position vectors and offsets for a three-rod subsegment, with hole positions defined by Eq. (25). This offset may then be added to the core's radius to determine the rod's radius of curvature, shown in Eq. (26).

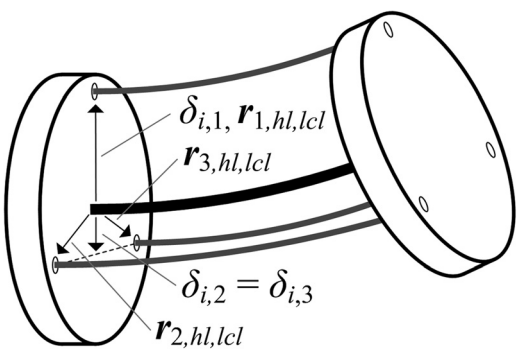

Fig. 4 Illustration of the radius offset for a case when $\varphi = 0$

$$\delta_{i,j} = \begin{bmatrix} c_{\varphi_i}, & s_{\varphi_i}, & 0 \end{bmatrix}^T \cdot \boldsymbol{r}_{j,\mathrm{hl,lcl}} \tag{24}$$

$$\begin{aligned} \boldsymbol{r}_{1,\mathrm{hl,lcl}} &= r_h\begin{bmatrix} 1, & 0, & 0 \end{bmatrix}^T, \\ \boldsymbol{r}_{2,\mathrm{hl,lcl}} &= r_h\begin{bmatrix} -0.5, & 0.5\sqrt{3}, & 0 \end{bmatrix}^T, \\ \boldsymbol{r}_{3,\mathrm{hl,lcl}} &= r_h\begin{bmatrix} -0.5, & -0.5\sqrt{3}, & 0 \end{bmatrix}^T \end{aligned} \tag{25}$$

$$1/k_{i,j} = 1/k_i - \delta_{i,j} \rightarrow k_{i,j} = k_i/\left(1 - k_i\delta_{i,j}\right) \tag{26}$$

The jth actuation rod bending moment magnitude $M_{i,j,\mathrm{bnd},r}$ of subsegment i is defined in Eq. (27), where E_r is the rod's Young's modulus and $J_{xx,r}$ is the rod cross section's second moment of area.

$$M_{i,j,\mathrm{bnd},r} = E_r J_{xx,r} k_{i,j} \tag{27}$$

The total bending moment $\boldsymbol{M}_{i,\mathrm{bnd}}$ of subsegment i is defined in Eq. (28). The magnitude of $\boldsymbol{M}_{i,\mathrm{bnd}}$ is the sum of the subsegment's core and rod elastic moment magnitudes, and the direction of $\boldsymbol{M}_{i,\mathrm{bnd}}$ is orthogonal to the bending plane defined by φ_i. The resulting elastic moment loading $\boldsymbol{M}_{i,\mathrm{el}}$ on each disk i is found using Eq. (29). Intermediate disks are loaded with the difference of the two adjacent subsegments' bending moments, while the terminal disk is loaded with the final subsegment's bending moment.

$$\boldsymbol{M}_{i,\mathrm{bnd}} = \left(M_{i,\mathrm{bnd},c} + \sum_j M_{i,j,\mathrm{bnd},r}\right)\boldsymbol{R}_{i-1}\begin{bmatrix} -s_{\varphi_i}, & c_{\varphi_i}, & 0 \end{bmatrix}^T \tag{28}$$

$$\boldsymbol{M}_{i,\mathrm{el}} = \begin{cases} \boldsymbol{M}_{i+1,\mathrm{bnd}} - \boldsymbol{M}_{i,\mathrm{bnd}} & i < n \\ -\boldsymbol{M}_{i,\mathrm{bnd}} & i = n \end{cases} \tag{29}$$

4.3 Gravitational Effects. The gravitational force $\boldsymbol{F}_{i,\mathrm{gr}}$ applied at each disk's center-of-mass is defined in Eq. (30), where g is the gravitational constant.

$$\boldsymbol{F}_{i,\mathrm{gr}} = -m_i g \boldsymbol{x}_0 \tag{30}$$

4.4 Actuation Loading: Contact Forces. Actuation loading accounts for the force and moment on each disk due to the axial force in each rod. In addition, the contact forces between disks and rods result in friction. The resulting forces on the disks are reformulated as a resultant force and moment at the disk center-of-mass.

The actuation forces applied may be considered as end forces and contact forces, as shown in Fig. 5. The end force $\boldsymbol{F}_{j,\mathrm{end}}$ is applied at the nth disk where actuation rod j terminates and

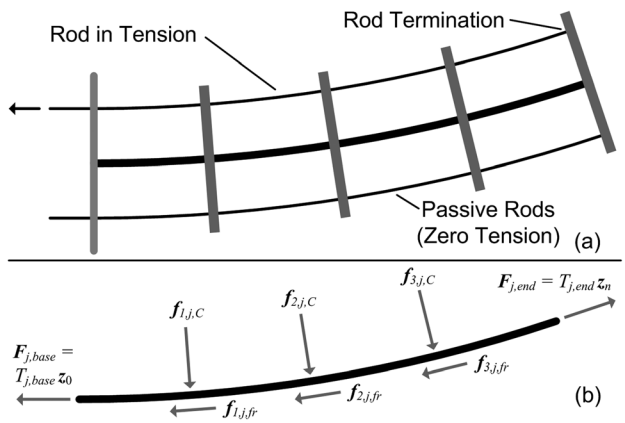

Fig. 5 (*a*) 2D projection of a single-segment rod-driven manipulator with the upper rod in tension and the two lower rods passive (zero axial force). (*b*) Free-body diagram of the rod under consideration with the applied force from the actuator, the end force from the rod's rigid connection to the end disk, and the contact forces parallel to the disks, normal to the rod and applied at the disk locations.

connects, defined in Eq. (31), where $T_{j,\text{end}}$ is the axial force at the end of rod j and $\boldsymbol{z}_n$ is the vector tangent to disk n. In the absence of friction, this force is calculable directly from the axial force input and robot geometry; with friction, this is no longer true.

$$\boldsymbol{F}_{j,\text{end}} = -T_{j,\text{end}}\boldsymbol{z}_n \tag{31}$$

The coupling of each rod's axial and the frictional forces complicates analysis. To compute each disk's friction, the contact force is needed. However, to compute the disks' contact forces, the friction forces are needed. Therefore, an iterative approach is used to converge on correct values. The starting point assumes the axial force is constant along the rod. From here, the contact forces are estimated for each rod. These contact force estimates are then used to calculate the frictional force at each disk. With these frictional forces, the end force will be updated, and the contact forces will be recalculated. Section 6 includes analysis on the "convergence" of the subsegment contact forces based on the iterations of this process and will determine the appropriate iteration count to ensure accurate computation in minimal steps.

The intermediate disk contact forces are calculated from the instantaneous static equilibrium of each actuation rod. It is assumed the dynamic effects of the rod's mass are negligible. Numerical optimization is used to determine the contact force magnitudes along the segment(s). A vector of the contact force magnitudes $f_{i,j,C}$ for the i intermediate disk-rod contacts on rod j is the optimization's input. The net equilibrium force $\boldsymbol{f}_{j,\text{eq}}$ is due to the summation of the contact and end forces, shown in Eq. (32), where $T_{j,\text{base}}$ is the axial force applied at the base and $\hat{f}_{i,j,C}$ is the direction of the contact force on rod j at disk i. The net equilibrium moment $\boldsymbol{m}_{j,\text{eq}}$ is calculated relative to the base of the rod, shown in Eq. (33), where $\boldsymbol{p}_{i,j,\text{rod}}$ is the rod-disk contact point position of the ith disk relative to the base of the rod. The rod j objective function $F_{j,\text{obj}}$ is the sum of squares resulting from $\boldsymbol{f}_{j,\text{eq}}$ and $\boldsymbol{m}_{j,\text{eq}}$, defined in Eq. (34). This model assumes the calculation of at least three contact forces will be required. Furthermore, as the number of contact forces increases beyond the number of terms contributing to the sum of squares, the null-space of the solution will increase, possibly enabling different sets of contact force magnitudes to minimize the objective function.

$$\boldsymbol{f}_{j,\text{eq}} = T_{j,\text{base}}\boldsymbol{z}_0 + \sum_{i=1}^{n-1}\left(f_{i,j,C}\hat{\boldsymbol{f}}_{i,j,C}\right) - T_{j,\text{end}}\boldsymbol{z}_n \tag{32}$$

$$\boldsymbol{m}_{j,\text{eq}} = \sum_{i=1}^{n-1}\left(\boldsymbol{p}_{i,j,\text{rod}} \times f_{i,j,C}\hat{\boldsymbol{f}}_{i,j,C}\right) - \boldsymbol{p}_{n,j,\text{rod}} \times \left(T_{j,\text{end}}\boldsymbol{z}_n\right) \tag{33}$$

$$F_{j,\text{obj}} = \boldsymbol{m}_{j,\text{eq}}^T\boldsymbol{m}_{j,\text{eq}} + \boldsymbol{f}_{j,\text{eq}}^T\boldsymbol{f}_{j,\text{eq}} \tag{34}$$

This null-space stems from the fact that the rod geometry is prescribed by the robot geometry, and the contact forces are calculated based on that geometry. In other nondeterministic static equilibrium calculations with a greater number of forces calculated than the number of equations of motion, a constitutive model is used to relate displacement to force, and the coupled forces and displacements are calculated. However, in this case, the displacements are specified, and the forces are calculated. In theory, a rod model could be generated with both the core and rod subsegment curvatures as coordinate variables, with compatibility conditions applied between the rods and cables, and coupled solutions of the rod forces and displacements. However, from a practical standpoint, this would significantly increase the number of coordinate variables in the model (for the robot in Fig. 1, the number of coordinates would jump from 16 to 72), likely making the solution intractable. Based on the cross-validation in Sec. 6, the optimization-based approach provides an acceptable level of accuracy. While this solution may depend on the initial condition of the optimization-based solver, by using this initial condition consistently during a dynamic simulation, the solution's consistency will be maintained and will continue to drive the solution toward the known steady-state configuration.

The contact force directions $\hat{\boldsymbol{f}}_{i,j,C}$ are calculated at each disk from the bending plane angle of the subsegment after the disk, shown in Eq. (35). The rod-disk contact point positions $\boldsymbol{p}_{i,j,\text{rod}}$ are found using Eqs. (36) and (37), where $\boldsymbol{r}_{i,j,\text{hl}}$ is the vector from the disk i origin to the rod j routing hole defined with respect to the base frame.

$$\hat{\boldsymbol{f}}_{i,j,C} = \boldsymbol{R}_i\begin{bmatrix} c_{\varphi_{i+1}} & s_{\varphi_{i+1}} & 0\end{bmatrix}^T \tag{35}$$

$$\boldsymbol{r}_{i,j,\text{hl}} = \boldsymbol{R}_i\boldsymbol{r}_{j,\text{hl,lcl}} \tag{36}$$

$$\boldsymbol{p}_{i,j,\text{rod}} = \boldsymbol{p}_i + \boldsymbol{r}_{i,j,\text{hl}} - \boldsymbol{r}_{j,\text{hl,lcl}} \tag{37}$$

Based on the model formulation, the contact force magnitudes that minimize F_{obj} equal the contact forces applied by the rod on the robot. Due to this, the actuation effects $\boldsymbol{F}_{i,\text{act}}$ and $\boldsymbol{M}_{i,\text{act}}$ may be calculated using Eqs. (38) and (39). Because the contact forces are parallel to the disk for $i < n$, the actuation moment on each disk is zero. However, when friction is considered in Sec. 4.4, there will be a contribution to the disk's actuation moment.

$$\boldsymbol{F}_{i,\text{act}} = \begin{cases} \sum_j f_{i,j,C}\hat{\boldsymbol{f}}_{i,j,C} & i < n \\ \sum_j \boldsymbol{F}_{j,\text{end}} & i = n \end{cases} \tag{38}$$

$$\boldsymbol{M}_{i,\text{act}} = \begin{cases} 0 & i < n \\ \sum_j \left(\boldsymbol{r}_{i,j,\text{hl}} \times \boldsymbol{F}_{j,\text{end}}\right) & i = n \end{cases} \tag{39}$$

4.5 Actuation Loading: Sliding Friction. The sliding friction arising from the disk-rod contact is calculable from the contact forces found in Sec. 4.3. However, the frictional forces will change the $T_{j,\text{end}}$ used to calculate those forces. An iterative approach is used to converge on the correct contact forces and friction. Static friction when the sliding velocity equals zero is neglected in the dynamic model for this first-stage work due to the difficulty in scaling the sliding velocity zero crossing detection for the numerous rod-disk contacts (e.g., 21 contact points for an eight-disk, single segment robot).

The conventional sliding friction model assumes friction $\boldsymbol{f}_{i,j,\text{fr}}$ is proportional to the contact force and opposes the sliding motion, defined in Eq. (40), where μ is the coefficient of sliding friction and $\dot{d}_{i,j,\text{dsk}}$ is the sliding velocity between the rod and disk.

$$\boldsymbol{f}_{i,j,\text{fr}} = \mu f_{i,j,C}\boldsymbol{z}_i \cdot \text{sgn}\left(\dot{d}_{i,j,\text{dsk}}\right) \tag{40}$$

Based on the friction force magnitudes in Eq. (40), the end axial force $T_{j,\text{end}}$ for each rod j is adjusted as shown in Eq. (41). The friction opposes the rod's motion: when pulled, the friction will reduce the axial force, and when pushed, the friction will increase the axial force.

$$T_{j,\text{end}} = T_{j,\text{base}} - \sum_i \mu f_{i,j,C}\text{sgn}\left(\dot{d}_{i,j,\text{dsk}}\right) \tag{41}$$

The sliding velocity $\dot{d}_{i,j,\text{dsk}}$ is calculable from the robot kinematics. The length $L_{i,j}$ of the ith subsegment of rod j and its derivative $\dot{L}_{i,j}$ are calculated using Eqs. (42) and (43). The sum of these rod subsegments velocities from a chosen disk to the rod's termination disk results in the chosen disk's rod sliding velocity, shown in Eq. (44).

$$L_{i,j} = k_i L_0/k_{i,j} \tag{42}$$

$$\dot{L}_{i,j} = L_0\left(k_{i,j}\dot{k}_i - k_i\dot{k}_{i,j}\right)/k_{i,j}^2 \tag{43}$$

$$\dot{d}_{i,j,\text{dsk}} = \begin{cases} 0 & i = n \\ \sum_{k=i+1}^{n} \dot{L}_{k,j}, & i < n \end{cases} \tag{44}$$

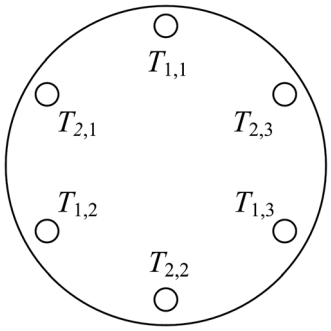

Fig. 6 Assignment of tension input variables to actuation transmission rods for a two-segment continuum robot with three rods per segment

Because the sliding friction model always opposes motion, the calculated friction is discontinuous when the velocity crosses zero. In this model, this discontinuity will cause an abrupt change in the loading on the disks, resulting in destabilization of the model. Therefore, a saturation function is used in place of the signum function to ensure friction remains continuous around the zero sliding velocity, as defined in Eq. (45), where $\dot{d}_{\text{sat}}$ is the saturation threshold velocity. A value of 0.05 m/s is used for the saturation velocity in this simulation.

$$\text{sat}\left(\dot{d}_{i,j,\text{dsk}}\right) = \begin{cases} \dot{d}_{i,j,\text{dsk}}/\dot{d}_{\text{sat}} & \left\|\dot{d}_{i,j,\text{dsk}}\right\| \leq \dot{d}_{\text{sat}} \\ \text{sgn}\left(\dot{d}_{i,j,\text{dsk}}\right) & \left\|\dot{d}_{i,j,\text{dsk}}\right\| > \dot{d}_{\text{sat}} \end{cases} \tag{45}$$

For the static model, there is no sliding motion. Therefore, the direction of the motion from an initial reference configuration to the static equilibrium position may be used to determine the direction of friction. Equation (46) defines the rod displacement $d_{i,j,\text{dsk}}$ for each rod j at disk i, assuming the rod moves from the zero-curvature (straight) configuration. As a result, for the static model, $\text{sgn}(\dot{d}_{i,j,\text{dsk}}) = \text{sgn}(d_{i,j,\text{dsk}})$.

$$d_{i,j,\text{dsk}} = \begin{cases} 0 & i = n \\ (n-i)L_0 - \sum_{k=i+1}^{n} L_{k,j} & i < n \end{cases} \tag{46}$$

The friction will also impact the calculation of the contact force magnitudes, due to the additional force effects on the rods during the calculation of their equilibrium. Equations (47) and (48) show the modification to Eqs. (32) and (33) due to friction.

$$\boldsymbol{f}_{j,\text{eq}} = T_{j,\text{base}}\boldsymbol{z}_0 + \sum_{i=1}^{n-1}\left(f_{i,j,C}\hat{\boldsymbol{f}}_{i,j,C} + \boldsymbol{f}_{i,j,\text{fr}}\right) - T_{j,\text{end}}\boldsymbol{z}_n \tag{47}$$

$$\boldsymbol{m}_{j,\text{eq}} = \sum_{i=1}^{n-1}\left[\boldsymbol{p}_{i,j,\text{rod}} \times \left(f_{i,j,C}\hat{\boldsymbol{f}}_{i,j,C} + \boldsymbol{f}_{i,j,\text{fr}}\right)\right] - \boldsymbol{p}_{n,j,\text{rod}} \times \left(T_{j,\text{end}}\boldsymbol{z}_n\right) \tag{48}$$

The resulting frictional forces will modify the force and moment loading on the robot by the rods. The new actuation force and moment are defined in Eqs. (49) and (50), respectively.

$$\boldsymbol{F}_{i,\text{act}} = \begin{cases} \sum_j \left(f_{i,j,C}\hat{f}_{i,j,C} + \boldsymbol{f}_{i,j,fr}\right) & i < n \\ \sum_j \boldsymbol{F}_{j,\text{end}} & i = n \end{cases} \tag{49}$$

$$\boldsymbol{M}_{i,\text{act}} = \begin{cases} \sum_j \left(\boldsymbol{r}_{i,j,\text{hl}} \times \boldsymbol{f}_{i,j,fr}\right) & i < n \\ \sum_j \left(\boldsymbol{r}_{i,j,\text{hl}} \times \boldsymbol{F}_{j,\text{end}}\right) & i = n \end{cases} \tag{50}$$

5 Multisegment Mechanics

In this section, the previous single-segment analyses for continuum robot modeling using the principle of virtual power is adapted for use in modeling multisegment robots. A key benefit of the chosen virtual power modeling method is the ease of scaling the model from a single-segment model to a multisegment model. The primary challenge is in the calculation of contact forces: instead of each rod interacting with each disk, different rods will have different numbers of contact points. Slight modifications to the calculation of inertial, elastic and gravitational loading are also necessary.

Before considering the mechanics of the multisegment manipulator, a systematic method of defining the structure in terms of its multiple segments is needed. As in the single-segment case, the model input is a vector of rod axial forces $\boldsymbol{T}$ arranged in two tiers: first by segment termination, then by counterclockwise position, as shown in Fig. 6. For the structure in Fig. 1, the input vector $\boldsymbol{T}$ is defined by Eq. (51), where T_{2-1} is the first rod terminating in the second segment. The local positions $\boldsymbol{r}_{i-j,\text{hl,lcl}}$ of the holes in the disk may be found for an N-segment manipulator with 3 rods per segment using Eq. (52) for the jth rod of the ith segment.

$$\boldsymbol{T} = \begin{bmatrix} T_{1-1} & T_{1-2} & T_{1-3} & T_{2-1} & T_{2-2} & T_{2-3} \end{bmatrix}^T \tag{51}$$

$$\begin{aligned} \boldsymbol{r}_{i-j,\text{hl,lcl}} &= r_h\begin{bmatrix} c_{\alpha_{i-j}}, & s_{\alpha_{i-j}}, & 0 \end{bmatrix}^T, \\ \alpha_{i-j} &= 2\pi(i-1)/3N + 2\pi(j-1)/3 \end{aligned} \tag{52}$$

For each segment, it is possible to define independent material (e.g., Young's modulus, density, etc.) and geometric (e.g., disk spacing, core diameter, etc.) properties. However, for this work it is assumed that properties are homogeneous along each segment (with the exception of the actuation transmission rods terminating at different disks). Given N segments and n subsegments per segment, the variable s is the product $s = N \cdot n$. The kinematics will be calculated as before, moving forward recursively from the base to the tip.

Table 1 Material and geometric properties of the experimental prototype. "P" denotes proximal segment and "D" denotes distal segment.

	Property	Value		Property	Value		Property	Value
m_i	Mass	P: $2.869\cdot10^{-3}$ (kg) D: $2.269\cdot10^{-3}$ (kg)	$I_{xx,\text{lcl}}$	Radial moment of inertia	P: $7.690\cdot10^{-6}$ (kg·m^2) D: $3.894\cdot10^{-6}$ (kg·m^2)	$I_{zz,\text{lcl}}$	Axial moment of inertia	P: $3.531\cdot10^{-7}$ (kg·m^2) D: $2.593\cdot10^{-7}$ (kg·m^2)
$J_{xx,c}$	Core second moment of area	$5.743\cdot10^{-14}$ (m^4)	$J_{xx,r}$	Rod second moment of area	$5.743\cdot10^{-14}$ (m^4)	L_0	Subsegment length (disk spacing)	30 (mm)
E_c	Core Young's modulus	$2.100\cdot10^{11}$ (Pa)	E_r	Rod Young's modulus	$2.100\cdot10^{11}$ (Pa)	g	Gravitational acceleration	9.81 (m/s^2)
r_h	Routing hole radius	12.5 (mm)	μ	Coefficient of friction	0.3	$\dot{d}_{\text{sat}}$	Velocity saturation limit	0.05 (m/s)

The calculation of the inertial, gravitational and elastic loading will be changed due to the variable number of rods in each subsegment between different sections. The bodies' masses and moments of inertia in the proximal segment are greater than those in the distal segment, due to the presence of six rods versus three. This requires a segment-by-segment calculation of inertial properties. Likewise, this will also impact the rod's elasticity. Six rods will contribute to the rods' elastic loading in the proximal segment, compared to three rods in the distal segment.

For actuation loading, the variable presence of the actuation transmission rods along the robot significantly impacts the loading in each segment. Specifically, the actuation rods that route through intermediate segments to their final segment will generate contact forces on the disks within these intermediate segments in addition to the rods that terminate in that segment. The contact force weighting for each rod will found independently for each rod. For example, in the two-segment, eight disk robot under consideration, for the first three rods, contact force magnitudes will be found for the rods' contacts with disks 1–3, and for the second three rods, contact force magnitudes will be found for the rods' contacts with disks 1–7.

6 Numerical Simulations and Cross-Validation

In this section, the virtual power continuum robot statics and dynamics models are implemented in MATLAB and case studies are presented to validate the model, including comparisons to dynamic FEA and experimental results.

6.1 Static and Dynamic Models. Static and dynamic models have been implemented in MATLAB using the "fsolve" function for the static model and the "ode45" function for the dynamic model. For the static model, the inertial effects $\boldsymbol{F}_{i,\text{inr}}$ and $\boldsymbol{M}_{i,\text{inr}}$ equal zero and the governing equation $\Delta P = 0$ is solved as a set of coupled algebraic equations.

To improve the convergence of the static model, a two-step solution process is programmed. First, the static model is solved for without contact forces, incorporating gravitational effects, elastic effects, and the end force actuation effects. This intermediate solution is then used as the initial condition for the full static model including contact forces and friction.

For the dynamic model, the inclusion of inertial effects results in a set of coupled second-order ODEs in time. In order to solve these equations using MATLAB, the equations must be re-organized into the form shown in Eq. (53), where $\boldsymbol{M}_{\text{wgt}}(\boldsymbol{q}, \dot{\boldsymbol{q}})$ is the weighting matrix and $\boldsymbol{V}_{\text{wgt}}(\boldsymbol{q}, \dot{\boldsymbol{q}})$ is the forcing vector.

$$\boldsymbol{M}_{\text{wgt}}\ddot{\boldsymbol{q}} = \boldsymbol{V}_{\text{wgt}} \tag{53}$$

To cast the equations in this form, the angular and linear accelerations are reformulated, taking the derivative of Eq. (2), resulting in Eq. (54). As a result, the inertial forces and moments take the form shown in Eq. (55).

$$\boldsymbol{\alpha}_i = \sum_k \left(\dot{\boldsymbol{\omega}}_{i,k}\dot{q}_k + \boldsymbol{\omega}_{i,k}\ddot{q}_k\right), \quad \boldsymbol{a}_i = \sum_k \left(\dot{\boldsymbol{v}}_{i,k}\dot{q}_k + \boldsymbol{v}_{i,k}\ddot{q}_k\right) \tag{54}$$

$$\begin{aligned} \boldsymbol{M}_{i,\text{inr}} &= -\boldsymbol{I}_i\boldsymbol{\omega}_{i,k}\ddot{\boldsymbol{q}}_k - \boldsymbol{I}_i\dot{\boldsymbol{\omega}}_{i,k}\dot{\boldsymbol{q}}_k - \boldsymbol{\omega}_i \times \boldsymbol{I}_i\boldsymbol{\omega}_i, \\ \boldsymbol{F}_{i,\text{inr}} &= -m_i\boldsymbol{v}_{i,k}\ddot{\boldsymbol{q}}_k - m_i\dot{\boldsymbol{v}}_{i,k}\dot{\boldsymbol{q}}_k \end{aligned} \tag{55}$$

With this new formulation for the inertial effects, the external forces and moments that will contribute to the weighting matrix ($\boldsymbol{M}_{i,\text{ex:}m}$ and $\boldsymbol{F}_{i,\text{ex:}m}$) and the forcing vector ($\boldsymbol{M}_{i,\text{ex:}v}$ and $\boldsymbol{F}_{i,\text{ex:}v}$) may be calculated as in Eq. (56). With these, $\boldsymbol{M}_{\text{wgt}}$ and $\boldsymbol{V}_{\text{wgt}}$ may be calculated using Eq. (4), as shown in Eq. (57). In addition, because "ode45" requires the ODEs as a single-order system, the second-order ODEs must be recast into the form shown in Eq. (58), where $\text{X} = \left[\boldsymbol{q}^T \quad \dot{\boldsymbol{q}}^T\right]^T$ and $\boldsymbol{I}$ is the identity matrix.

$$\begin{aligned} \boldsymbol{M}_{i,\text{ex:}m} &= \boldsymbol{I}_i\boldsymbol{\omega}_{i,k}, \quad \boldsymbol{F}_{i,\text{ex:}m} = m_i\boldsymbol{v}_{i,k}, \\ \boldsymbol{M}_{i,\text{ex:}v} &= -\boldsymbol{I}_i\dot{\boldsymbol{\omega}}_{i,k}\dot{\boldsymbol{q}}_k - \boldsymbol{\omega}_i \times \boldsymbol{I}_i\boldsymbol{\omega}_i + \boldsymbol{M}_{i,\text{el}} + \boldsymbol{M}_{i,\text{act}}, \\ \boldsymbol{F}_{i,\text{ex:}v} &= -m_i\dot{\boldsymbol{v}}_{i,k}\dot{\boldsymbol{q}}_k + \boldsymbol{F}_{i,\text{gr}} + \boldsymbol{F}_{i,\text{act}} \end{aligned} \tag{56}$$

$$\begin{aligned} \boldsymbol{M}_{\text{wgt}} &= \sum_i \left(\boldsymbol{\omega}_{i,k} \cdot \boldsymbol{M}_{i,\text{ex:}m} + \boldsymbol{v}_{i,k} \cdot \boldsymbol{F}_{i,\text{ex:}m}\right) \\ \boldsymbol{V}_{\text{wgt}} &= \sum_i \left(\boldsymbol{\omega}_{i,k} \cdot \boldsymbol{M}_{i,\text{ex:}v} + \boldsymbol{v}_{i,k} \cdot \boldsymbol{F}_{i,\text{ex:}v}\right) \end{aligned} \tag{57}$$

$$\begin{bmatrix} \boldsymbol{I} & \boldsymbol{0} \\ \boldsymbol{0} & \boldsymbol{M}_{\text{wgt}} \end{bmatrix} \dot{X} = \begin{bmatrix} \dot{\boldsymbol{q}} \\ \boldsymbol{V}_{\text{wgt}} \end{bmatrix} \tag{58}$$

In both models there is a need to solve for the contact forces magnitudes, as discussed in Sec. 4.3. MATLAB's "lsqnonlin" function is used to solve the optimization presented in that section. Use of "lsqnonlin" is permissible because the objective function F_{obj} is a sum of square terms. To improve convergence, in addition to the calculation of $\boldsymbol{f}_{j,\text{eq}}$ and $\boldsymbol{m}_{j,\text{eq}}$ for the objective function, the Jacobian of these terms with respect to the contact force magnitudes is provided. The ith column of the objective function vector Jacobian $\boldsymbol{J}_{j,\text{obj}}$ is defined in Eq. (59). To improve convergence, in cases where planar actuation is prescribed by the input axial forces, the second, fourth and sixth terms are ignored and the sum of squares and Jacobian will depend only on the x- and z-forces and y-moment.

$$\boldsymbol{J}_{j,\text{obj}}(:,i) = \left[\hat{\boldsymbol{f}}_{i,C}^T, \quad \left(\boldsymbol{p}_{i,j,\text{rod}} \times \hat{\boldsymbol{f}}_{i,C}\right)^T\right]^T \tag{59}$$

For the simulations in the following sections, two sets of initial conditions are used. For the zero-actuation case study, the initial β_i is $-0.001\,\text{m}^{-1}$ and the initial γ_i is 0 to avoid the singularity in the calculation of $\boldsymbol{p}_{i,\text{lcl}}$ and its derivatives when $\beta_i = \gamma_i = k_i = 0$. For the actuated simulations, the initial condition is the continuum robot's zero actuation static equilibrium. For all case studies, the robot has the material and geometric properties detailed in Table 1.

6.2 Frictional Force Iteration Validation. As discussed in Secs. 4.3 and 4.4, the contact and friction forces calculations are coupled. An algorithm was provided capable of sequentially calculating the properties; however, the minimal number of iterations to be performed is required. Based on prototype construction for the experimental validation, a maximum axial force of 30 N was set for the simulations and experiments.

Figure 7 shows the convergence of the contact force magnitudes in two cases: (1) planar actuation of the proximal segment with $T_{1,1} = 30\,\text{N}$ and (2) planar actuation of the whole robot with $T_{2,2} = 30\,\text{N}$. During preliminary simulations, planar actuation was found to converge in more steps than spatial actuation because of the fewer degrees of freedom present for the optimization (three terms in the objective function versus six) of the contact force magnitudes. Furthermore, during preliminary simulations, it was found that the convergence rate increases as the force magnitude

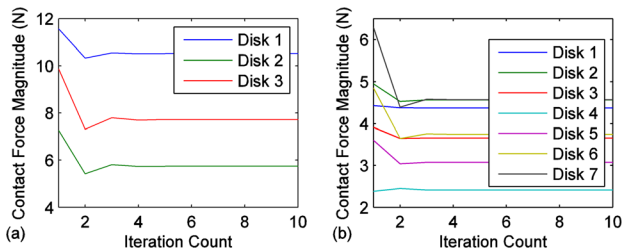

Fig. 7 Convergence of contact force magnitudes for a two segment, eight-disk continuum robot. (*a*) $T_{1,1}$ actuated with 30 N (rod connects at disk 4). (*b*) $T_{2,2}$ actuated with 30 N (rod connects at disk 8).

Table 2 Maximum contact force magnitude error for each iteration for static simulations with $T_{1,1} = 30\,\text{N}$ or $T_{2,2} = 30\,\text{N}$

Iter.	Error (%)	Iter.	Error (%)	Iter.	Error (%)
1	$T_{1,1}$: 27.9 $T_{2,2}$: 37.8	4	$T_{1,1}$: 2.21×10^{-1} $T_{2,2}$: 8.96×10^{-3}	7	$T_{1,1}$: 1.68×10^{-3} $T_{2,2}$: 8.42×10^{-8}
2	$T_{1,1}$: 5.71 $T_{2,2}$: 3.91	5	$T_{1,1}$: 4.34×10^{-2} $T_{2,2}$: 2.13×10^{-4}	8	$T_{1,1}$: 3.16×10^{-4} $T_{2,2}$: 2.24×10^{-8}
3	$T_{1,1}$: 1.12 $T_{2,2}$: 2.32×10^{-1}	6	$T_{1,1}$: 8.50×10^{-3} $T_{2,2}$: 2.76×10^{-6}	9	$T_{1,1}$: 7.71×10^{-5} $T_{2,2}$: 2.20×10^{-9}

increases. Table 2 shows the maximum percent error at each iteration of the contact force magnitude relative to the final result at iteration 10 for the two cases. While the segment 2 simulation has higher initial error, it more quickly converges to the final contact force. Therefore, the segment 1 modeling dictates the minimum number of iterations. As seen in Table 2, six iterations results in a solution with less than a 1% difference from the final value. Therefore, in all simulations, six iterations will be utilized.

6.3 Dynamic Responses. Dynamic simulations were generated using the virtual power model for three case studies: (1) zero actuation in the rods, (2) rod 1-1 actuated with a 10 N tension, and (3) rod 2-2 actuated with a 10 N tension. Figure 8 illustrates the dynamic response of the β curvatures of the continuum robot's subsegments with zero axial force in the rods. The simulation results in sustained oscillations of the continuum robot's curvatures around a stable point. Because the axial forces are all zero, there is no contact force between the rods and disks, resulting in zero friction along the arm. In this case, the rod's bending is due to the moment applied by the terminal disk and transmitted along the rod. The elastic effects of these passive rods are then incorporated into the $\boldsymbol{M}_{i,\text{el}}$ term. Because sliding friction due to the contact forces is the only dissipative force in the model, the vibrations are not dampened and remain sustained over the interval.

Figure 9 illustrates the dynamic response of the robot with rod 1-1 (Fig. 6, the first rod that terminates in the first segment) actuated with a tension of 10 N. Because the actuation remains in-plane, only the β curvatures are nonzero. In addition, due to the contact forces between the actuation rods and the disks, friction dampens the responses. Because rod 1-1 terminates at disk 4, only subsegments 1–4 will have appreciably different steady-state curvature values. However, all subsegments experience vibration attenuation. For segment 1, this is due to the contact friction between rod 1-1 and the disks adjacent to its subsegments. However, for segment 2, the dissipation is "indirect" due to the internal force loading of segment 1 on segment 2. When the segment 2 internal forces and moments are applied to segment 1, the frictional force will oppose the resulting motion. This frictional opposition results in reduction of the internal forces and moments, which results in reduced vibrations in segment 2.

The actuation of the segment 2 rods results in deformation along the entire robot, due to their routing through the proximal segment 1. Figure 10 illustrates the dynamic response of the continuum robot with rod 2-2 (Fig. 6, the second rod that terminates in the second segment) actuated with a tension of 10 N (same as the segment 1 dynamic response) from the initial condition of the zero actuation static equilibrium.

6.4 Static Versus Dynamic Virtual Power Model Comparison. As an initial point of comparison, the steady-state component of the dynamic virtual power model response (i.e., the constant values of the response around which the transient response oscillates) can be compared to the equilibrium configuration calculated by the static virtual power model. Figure 11 compares these for a 10 N tension in rod 1-1. As shown, they are nearly identical. The maximum position error is 0.2939% in disk 8, enabling interchangeable use of the static equilibrium model for the steady-state component of the dynamic response.

Figure 12 compares the dynamic model steady-state response to the static model equilibrium for actuation of rod 2-2 with 10 N tension. Although there is slightly more variation between these two configurations than in Fig. 11, the maximum error in disk 8

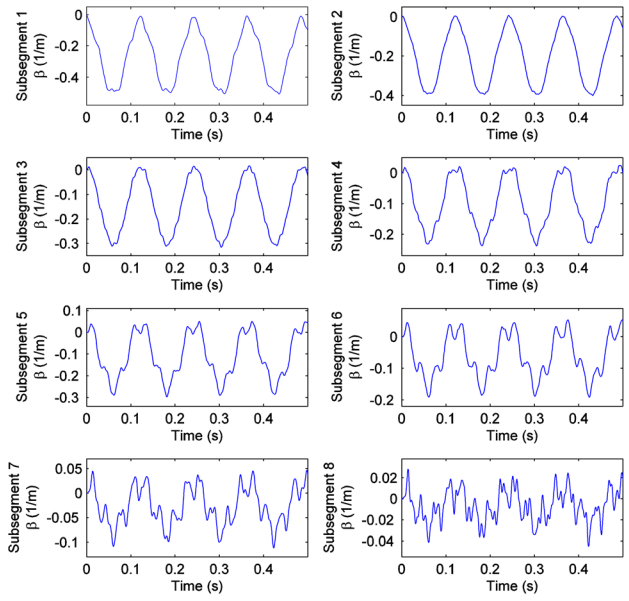

Fig. 8 Zero actuation virtual power dynamic model response β curvatures. These curvature profile correspond to tip oscillations with peak-to-peak amplitude of 9.48 mm around $x = -4.74$ mm.

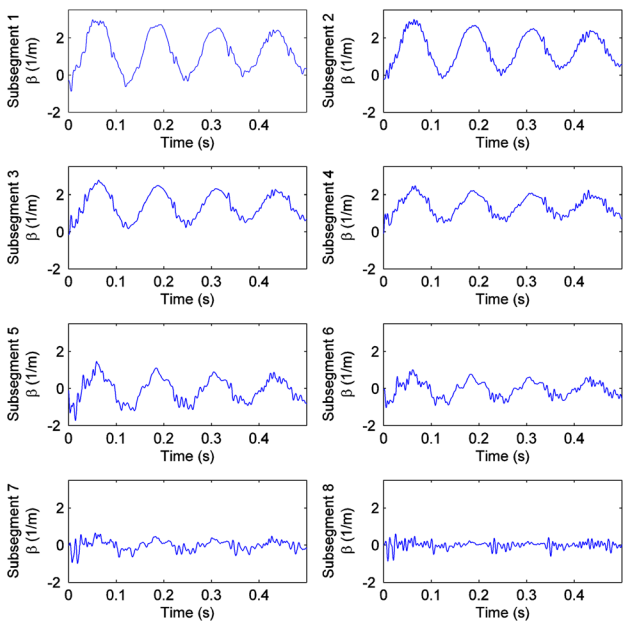

Fig. 9 Rod 1-1 actuation (10 N) dynamic virtual power model β curvature responses

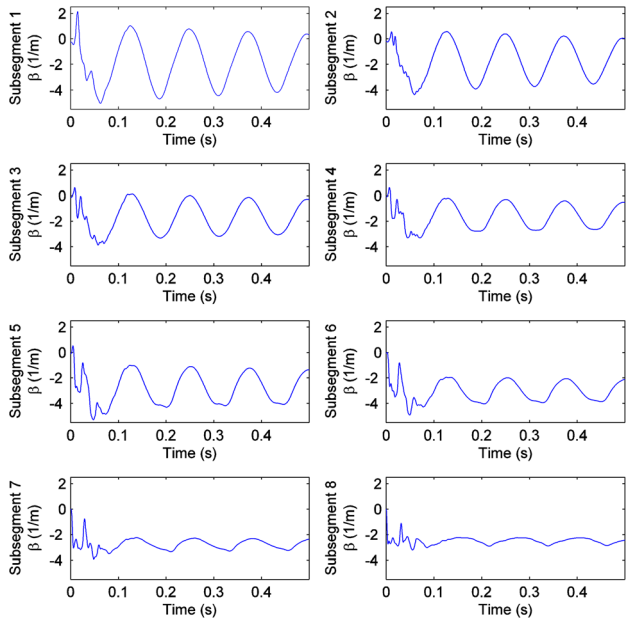

Fig. 10 Rod 2-2 actuation (10 N) dynamic virtual power model β curvature responses

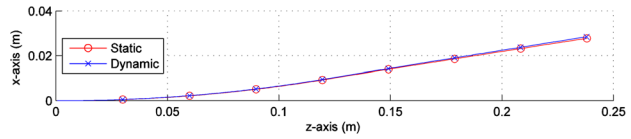

Fig. 11 Comparison of the calculated static virtual power model equilibrium to the steady-state component of the dynamic virtual power model response for actuation of 10 N in rod 1-1

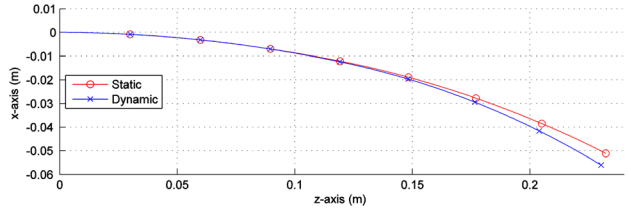

Fig. 12 Comparison of the calculated static virtual power model equilibrium to the steady-state component of the dynamic virtual power model response for actuation of 10 N in rod 2-2

Table 3 Percent error of dynamic response steady-state component relative to static equilibrium for actuation of 10 N in rod 2-2

Disk	Error (%)	Disk	Error (%)	Disk	Error (%)
1	0.0735	4	0.2448	7	1.5957
2	0.0684	5	0.5221	8	2.2165
3	0.0502	6	0.9805	—	—

position is still 2.2165%, or 5.3 mm. Table 3 provides the error of the steady-state dynamic response component relative to the static equilibrium. In addition, it is seen that for identical tension inputs, the segment 2 rods will cause greater overall deflection.

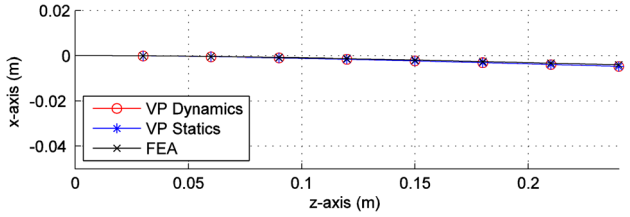

Fig. 13 Comparisons of the zero actuation dynamic virtual power model response steady-state component to the calculated equilibria using the static virtual power model and the static finite element analysis model

6.5 Finite Element Analysis Validation of Virtual Power Model. Two properties of the zero actuation dynamic response shown in Fig. 8 have been analyzed: the magnitude of the steady-state component and the frequency response of the transient component. Figure 13 compares the dynamic response's steady-state component to: (1) the static virtual power model equilibrium, and (2) the equilibrium of a static FEA model of the continuum robot. This FEA model was generated using COMSOL's Structural Mechanics model using the geometric and material properties detailed in Table 1. A 3D linear elasticity material model was chosen, and the geometry was discretized using a "Fine" mesh. As shown in Fig. 13, the three plots are practically superimposed on one another. The maximum disk position error for both the dynamic response steady-state component and the static equilibrium model relative to the FEA simulation is 0.2958%.

The frequency response of the virtual power dynamic response was compared to a dynamic FEA simulation in COMSOL. A fast Fourier transform using MATLAB was performed on the oscillations of the x-components of displacement of the disks' centers-of-mass to quantify the frequency response. For the dynamic virtual power model, the curvature responses illustrated in Fig. 8 were mapped into disk trajectories, based on the kinematic analysis in Sec. 3.

Figure 14 illustrates the frequency responses of the first and eighth disk in the robot. As illustrated, the frequency response profiles' shapes between the two disks' oscillations are similar and differ primarily in their magnitudes. However, there is a slight difference in the peak frequency of the first mode: the FEA simulation exhibits a greater fundamental frequency (9.76 Hz) than the virtual power model (7.81 Hz). This is primarily due to the difference in discretization between the two models: the dynamic virtual power model is defined by 32 variables, whereas the FEA uses a model composed of 6964 elements. In addition, the model discretization makes several assumptions for model simplicity that change the mass properties of the robot. The first half of the core and rods in subsegment 1 are not explicitly modeled, due to

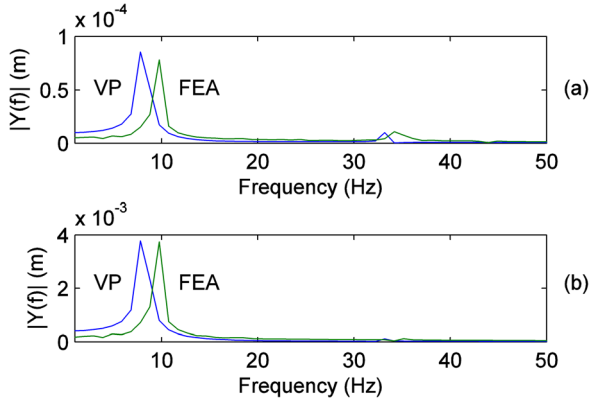

Fig. 14 Comparison of frequency response of vertical displacements of (*a*) disk 1 and (*b*) disk 8 from VP and FEA simulations

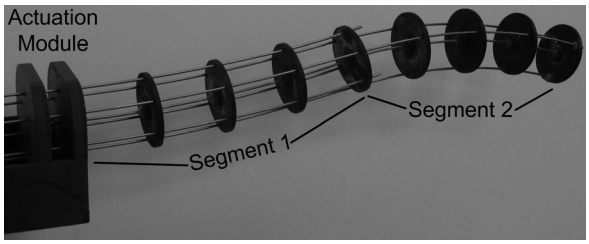

Fig. 15 Rod-driven, two-segment prototype used for validating actuated case studies

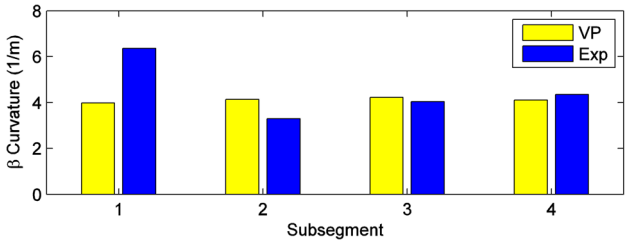

Fig. 17 Comparison of β curvatures for subsegments 1–4 for the experimentally measured static equilibrium and the calculated static virtual power model equilibrium for 30 N tension in rod 1-1

the lumping of these masses elsewhere with their immediately surrounding disks. On the other hand, at disk 4, the mass properties are assumed to be the same as the three previous disks, but one triplet of rods does not continue past disk 4. Likewise, at disk 8, rods are modeled as continuing beyond the disk, when in actuality they do not. The redistribution of this mass would have an effect on the dynamic properties of the robot and likely contributes to this error.

6.6 Experimental Validation of Virtual Power Model. Experimental validation is used to verify the accuracy of the actuated case studies of the virtual power model. Figure 15 shows the experimental test platform utilized. A spring steel core (ASTM A228, 1.04 mm diameter, 240 mm long) was used with eight disks (ABS plastic, 30 mm diameter, 2 mm thick, 30 mm disk spacing) mounted along the core using cyanoacrylate (Loctite 401). The actuation rods are also spring steel (ASTM A228, 1.04 mm diameter), route through holes in the disk of 1.75 mm diameter, and terminate and are connected to the fourth or eighth disk using the above cyanoacrylate. Hanging weights are used to tension the rods, with an adapter mounted on the rod with polytetrafluoroethylene-coated fiberglass thread tied on and routed over a spool supported by ball bearings. The actuation rods were routed through the disks offset 12.5 mm from the center (Fig. 2 shows the arrangement). The properties of this prototype match the properties used in the numerical models shown in Table 1.

The shape was measured by photographing the disks in profile, then indirectly calculating the curvature from the relative angle between the two disks adjacent to each subsegment. The bending plane angle θ_i was found for each subsegment by subtracting the two adjacent disks' angles, and the subsegment curvature was found by dividing θ_i by L_0. The error of this image processing step was estimated by determining the angle of gradations on a protractor, then determining the associated curvature for each given difference in angle. This was compared to the predicted curvature for the known difference in angle. The maximum curvature error was found to be 1.637%.

Figure 16 compares the experimentally measured continuum robot static equilibria to the calculated static equilibria from the virtual power model for tensions of 10, 20, and 30 N applied to rod 1-1. In each case, a pattern is observed where for each tension, the experimental results exhibit greater curvature in subsegment 1 than the virtual power simulation, reduced curvature in subsegment 2 compared to the virtual power simulation, and similar curvatures for subsegments 3 and 4, as shown in Fig. 17. This is due primarily to the assumption in the model that the actuation rods are held horizontal at the base of the robot. In the experimental prototype, the clearance between the routing holes for the rods allows for slight variation from horizontal. As a result, the elastic loading in the model is greater than the actual elastic loading in the prototype. This could be compensated for by adjusting the assumed boundary condition of the model at the base of the robot; this and other improvements to the model based on prototype construction will be discussed in Sec. 7. However, even with this slight discrepancy, the errors of the modeled positions of the disks relative to the experimental results are all still less than 5%, with a maximum error of 4.89% occurring in disk 8 for the 30 N case.

Figure 18 compares the experimentally measured static equilibria to the calculated static equilibria from the virtual power model for tensions of 5, 10, and 15 N in rod 2-2. As seen in Fig. 16, the reduced elastic moment generated in subsegment 1 seen in the experimental prototype causes the measured configuration to consistently extend beyond the predicted shape. The maximum disk position error of 5.53% is seen in disk 8 for the 10 N actuation case.

The mutual actuation of rods 1-1 and 2-2 results allows for the quasi-independent control of these two segments. To validate this model, the impact of segment 2 loading on a robot with fixed segment 1 loading was considered. Rod 1-1 was tensioned with 25 N, and the tension in rod 2-2 was varied from 5 N to 15 N. Because of the previously demonstrated correlation between the steady-state component of the dynamic responses and the static equilibria, the static models are directly compared to the experimental results generated for the previously described loading conditions. Figure 19 illustrates the resulting experimental results and calculated static equilibria for the loading described above. The maximum error occurs of 8.02% occurs in disk 7 of the 5 N actuation case.

The neglect of torsion in this model leads to out-of-plane actuation cases being very similar to the planar cases. As discussed in

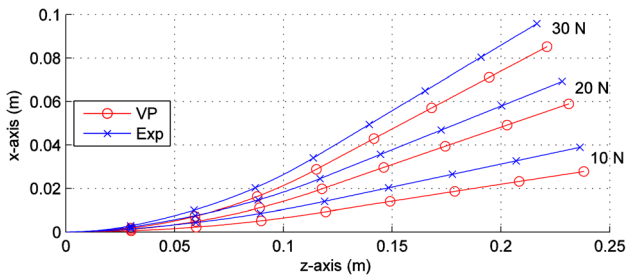

Fig. 16 Comparison of the experimentally measured static equilibrium and the calculated static virtual power model equilibrium for tensions of 10, 20, and 30 N in rod 1-1

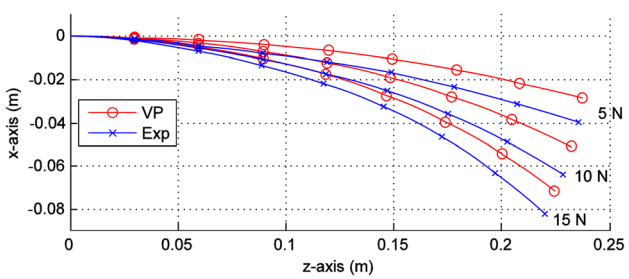

Fig. 18 Comparison of the experimentally measured static equilibrium and the calculated static virtual power model equilibrium for tensions of 5, 10, and 15 N in rod 2-2

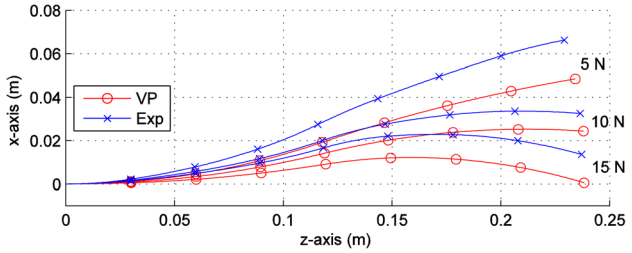

Fig. 19 Comparison of the experimentally measured static equilibrium and the calculated static virtual power model equilibrium for a tension of 25 N in rod 1-1 and tensions of 5, 10, and 15 N in rod 2-2

Sec. 7, in future work with larger and longer continuum robots, the impact on torsion of out-of-plane loading will be studied and accounted for in the virtual power model.

In addition, experimental validation of the transient behavior of the dynamic model is also an element of the future work due to the dependence of the continuum robot prototype's dynamic response on the actuation mechanism. In the current model, step functions are used to apply constant tension forces to the rods. However, the system inputs for an experimental prototype would likely be displacement set points for linear actuators driving the rods. As a result, the force profiles applied by these linear actuators would be significantly different than step functions. Experimental validation of the transient continuum robot response will be a key element of verifying the accuracy of the integrated actuation mechanism and continuum robot model.

7 Conclusion

This paper presented a novel approach using the principle of virtual power to model the mechanics of rod-driven continuum robots, with considerations for both multisegment structures and friction between the actuation rods and disks. The resulting static equilibrium model was a series of coupled algebraic equations capable of being solved numerically, and the resulting dynamic response model was a set of weighted ordinary differential equations capable of being numerically integrated. The modeling approach was validated by comparing the simulated zero actuation, in-plane actuation and out-of-plane actuation dynamic responses to the static virtual power model, dynamic FEA and experimental results.

Future work associated with this topic includes studies into quantifying and improving numerical model efficiency, improving the mechanics model, and applying the model for task planning and control. In terms of improving numerical efficiency, the key first step will be to implement the model in a lower-level language than MATLAB m-code, such as C. Then, other dynamic models would need to be implemented in a similar fashion and their performance compared. In terms of improvements to the mechanics model, the next key step is incorporating torsional effects into the rod-driven model to account for the "twist" due to out-of-plane loading from gravitational effects in large-scale continuum robots. In addition, robot-specific adjustments and improvements to the model will need to be considered, such as (1) modeling the mechanics of an actuation module to enable mapping between the robot's actual control inputs (e.g., linear actuator displacement or motor torque) and the resulting shape, or (2) including local perturbations in boundary conditions due to tolerances in construction (e.g., the segment 1 elasticity modification discussed in Sec. 6.3). Third, an alternative approach for incorporating the rod elasticity will be considered in which the rod elasticity is included in the rod equilibrium calculation, and its effect on the continuum robot shape will be applied through the contact forces.

In terms of task planning, we aim to formulate methods of inverse dynamics in which the intrinsic coupling between configuration (kinematics) and forces (kinetics) is accounted for. Unlike conventional rigid-structure robots, the joint-angle profiles may not be calculated separately from the joint torques required to realize them: they are intrinsically coupled. In terms of control, we aim to apply the virtual power method of mechanics modeling into a predictive controller capable of improving the stability of continuum arms by accounting for the vibrational modes of the structure. In addition, the discretization of this representation will enable better control of manipulator contact, particularly deformation around obstacles. Because each actuated segment it not required to exhibit a single mode shape in response to loading, more complex shapes may be adopted in response to environmental contact.

Acknowledgment

This material is based upon work supported by the National Science Foundation under Grant No. 1334227.

Nomenclature

$\boldsymbol{a}_i$ = disk i center-of-mass linear acceleration
$\boldsymbol{b}_{i,\mathrm{lcl}}$ = frame i local binormal vector relative to frame $i-1$
c = cosine (angle given as subscript)
$d_{i,j,\mathrm{dsk}}$ = rod displacement through hole j of disk i
d_{sat} = threshold sliding velocity for saturation function
E_c = elastic core Young's modulus
E_r = actuation rod Young's modulus
$f_{i,j,C}$ = contact force magnitude at disk i for rod j
$\boldsymbol{f}_{i,j,C}$ = contact force at disk i for rod j
$\boldsymbol{f}_{i,j,\mathrm{fr}}$ = friction force at hole j on disk i
$\boldsymbol{f}_{j,\mathrm{eq}}$ = net equilibrium force on rod j
$\boldsymbol{F}_{i,\mathrm{act}}$ = disk i actuation force
$\boldsymbol{F}_{i,\mathrm{ex}}$ = disk i total external force
$\boldsymbol{F}_{i,\mathrm{ex}:m}$ = matrix component of disk i total external force
$\boldsymbol{F}_{i,\mathrm{ex}:v}$ = vector component of disk i total external force
$\boldsymbol{F}_{i,\mathrm{gr}}$ = disk i gravitational force
$\boldsymbol{F}_{i,\mathrm{inr}}$ = disk i inertial force
$\boldsymbol{F}_{j,\mathrm{end}}$ = force applied by rod j on terminating disk
$F_{j,\mathrm{obj}}$ = objective function for rod j static equilibrium optimization
g = gravitational constant
$\boldsymbol{I}$ = identity matrix
$\boldsymbol{I}_i$ = disk i global moment of inertia
$\boldsymbol{I}_{i,\mathrm{lcl}}$ = disk i local moment of inertia
$I_{i,xx,\mathrm{lcl}}$ = disk i radial moment of inertia aligned with $\boldsymbol{n}_{i,\mathrm{lcl}}$ axis
$I_{i,yy,\mathrm{lcl}}$ = disk i radial moment of inertia aligned with $\boldsymbol{b}_{i,\mathrm{lcl}}$ axis
$I_{i,zz,\mathrm{lcl}}$ = disk i axial moment of inertia aligned with $\boldsymbol{t}_{i,\mathrm{lcl}}$ axis
$J_{j,\mathrm{obj}}$ = objective function vector Jacobian
$J_{xx,c}$ = elastic core cross section second moment of area
$J_{xx,r}$ = actuation rod cross section second moment of area
k_i = subsegment i curvature magnitude
$k_{i,j}$ = curvature magnitude of rod j in subsegment i
$L_{i,j}$ = length of subsegment i rod j
L_0 = spacing between disks
m_i = disk i mass
$\boldsymbol{M}_{i,\mathrm{act}}$ = disk i actuation moment
$\boldsymbol{M}_{i,\mathrm{bnd}}$ = subsegment i bending moment
$M_{i,\mathrm{bnd},c}$ = subsegment i core bending moment magnitude
$\boldsymbol{M}_{i,\mathrm{el}}$ = disk i elastic moment
$\boldsymbol{M}_{i,\mathrm{ex}}$ = disk i total external moment
$\boldsymbol{M}_{i,\mathrm{ex}:m}$ = matrix component of disk i total external moment
$\boldsymbol{M}_{i,\mathrm{ex}:v}$ = vector component of disk i total external moment
$\boldsymbol{M}_{i,\mathrm{inr}}$ = disk i inertial moment
$M_{i,j,\mathrm{bnd},r}$ = subsegment i rod j bending moment magnitude
$\boldsymbol{m}_{j,\mathrm{eq}}$ = net moment of rod j relative to base
$\boldsymbol{M}_{\mathrm{wgt}}$ = weighting matrix for second-order ODE model
$\boldsymbol{n}_{i,\mathrm{lcl}}$ = frame i local normal vector relative to frame $i-1$

P = total virtual power
$\boldsymbol{p}_i$ = disk i center of mass position vector relative to origin of base frame
$\boldsymbol{p}_{i,j,\text{rod}}$ = disk i hole j position vector relative to origin of base frame
$\boldsymbol{p}_{i,\text{lcl}}$ = disk i center of mass local position vector relative to origin of frame $i-1$
$\boldsymbol{q}_{i,\text{lcl}}$ = subsegment i coordinates
q_k, $\boldsymbol{q}$ = generalized coordinates
r_h = rod routing hole distance from disk origin
$\boldsymbol{R}_i$ = frame i orientation relative to base frame
$\boldsymbol{r}_{i,j,\text{hl}}$ = position vector from disk i origin to hole j defined with respect to base frame
$\boldsymbol{r}_{i-j,\text{hl,lcl}}$ = segment i rod j local hole position vector
$\boldsymbol{R}_{i,\text{lcl}}$ = frame i local orientation relative to frame $i-1$
$\boldsymbol{r}_{j,\text{hl,lcl}}$ = rod j local hole position vector
s = sine (angle given as subscript)
$\boldsymbol{T}$ = input tension vector
$\boldsymbol{t}_{i,\text{lcl}}$ = frame i local tangent vector relative to frame $i-1$
T_{i-j} = input tension for rod j terminating in segment i
$T_{j,\text{base}}$ = axial force applied at base of rod j
$T_{j,\text{end}}$ = axial force of rod j at terminating disk
$\boldsymbol{v}_i$ = disk i center-of-mass linear velocity
$\boldsymbol{v}_{i,k}$ = disk i center-of-mass partial linear velocity for generalized coordinate k
$\boldsymbol{V}_{\text{wgt}}$ = forcing vector for second-order ODE model
$\boldsymbol{X}$ = state vector of generalized coordinates and velocities
$\hat{\boldsymbol{x}}$ = denotes unit vector
$\dot{x}, \ddot{x}$ = denotes first, second derivative in time
$\boldsymbol{x}_i$, $\boldsymbol{y}_i$, $\boldsymbol{z}_i$ = unit vectors defining global frame
$\boldsymbol{x}_0$, $\boldsymbol{y}_0$, $\boldsymbol{z}_0$ = unit vectors defining base frame
$\boldsymbol{\alpha}_i$ = disk i angular acceleration
α_{i-j} = segment i rod j hole position angle
β_i = subsegment i x-z plane curvature
γ_i = subsegment i y-z plane curvature
$\delta_{i,j}$ = radius of curvature offset for rod j in subsegment i
Δ = variation operator
θ_i = subsegment bending angle
μ = coefficient of sliding friction
φ_i = subsegment i bending plane angle
$\boldsymbol{\omega}_i$ = disk i angular velocity
$\boldsymbol{\omega}_{i,k}$ = disk i partial angular velocity for generalized coordinate k
$\boldsymbol{\omega}_{i,\text{lcl}}$ = disk i local angular velocity relative to frame $i-1$

References

[1] Trivedi, D., Rahn, C. D., Kier, W. M., and Walker, I. D., 2008, "Soft Robotics: Biological Inspiration, State of the Art, and Future Research," Appl. Bionics Biomech., **5**(3), pp. 99–117.
[2] McMahan, W., Jones, B. A., and Walker, I. D., 2005, "Design and Implementation of a Multi-Section Continuum Robot: Air-Octor," IEEE/RSJ International Conference on Intelligent Robots and Systems (IROS 2005), Alberta, Canada, August 2–6, pp. 2578–2585.
[3] Camarillo, D. B., Milne, C. F., Carlson, C. R., Zinn, M. R., and Salisbury, J. K., 2008, "Mechanics Modeling of Tendon-Driven Continuum Manipulators," IEEE Trans. Rob., **24**(6), pp. 1262–1273.
[4] Mao Y., and Agrawal S. K., 2012, "Design of a Cable-Driven Arm Exoskeleton (CAREX) for Neural Rehabilitation," IEEE Trans. Rob., **28**(4), pp. 922–931.
[5] Zhang, J., and Simaan, N., 2013, "Design of Underactuated Steerable Electrode Arrays for Optimal Insertions," ASME J. Mech. Rob., **5**(1), p. 011008.
[6] Xu, K., and Simaan, N., 2008, "An Investigation of the Intrinsic Force Sensing Capabilities of Continuum Robots," IEEE Trans. Rob., **24**(3), pp. 576–587.
[7] Simaan, N., Taylor, R., and Flint, P., 2004, "A Dexterous System for Laryngeal Surgery," IEEE International Conference on Robotics and Automation (ICRA '04), New Orleans, LA, April 26–May 1, pp. 351–357.
[8] Godage, I. S., Branson, D. T., Guglielmino, E., Medrano-Cerda, G. A., and Caldwell, D. G., 2011, "Dynamics for Biomimetic Continuum Arms: A Modal Approach," IEEE International Conference on Robotics and Biomimetics (ROBIO), Phuket, Thailand, December 7–11, pp. 104–109.
[9] McMahan, W., Chitrakaran, V., Csencsits, M. A., Dawson, D. M., Walker, I. D., Jones, B. A., Pritts, M., Dienno, D., Grissom, M., and Rahn, C. D., 2006, "Field Trials and Testing of the OctArm Continuum Manipulator," IEEE International Conference on Robotics and Automation (ICRA 2006), Orlando, FL, May 15–19, pp. 2336–2341.
[10] "Bionic Handling Assistant," 2010, Festo AG & Co. KG, Esslingen, Germany, accessed September 10, 2013, http://www.festo.com/net/SupportPortal/Files/42050/Brosch_FC_BHA_3_0_EN_lo.pdf
[11] De Volder, M., and Reynaerts, D., 2010, "Pneumatic and Hydraulic Microactuators: A Review," J. Micromech. Microeng., **20**(4), p. 043001.
[12] Lock, J., Laing, G., Mahvash, M., and Dupont, P. E., 2010, "Quasistatic Modeling of Concentric Tube Robots With External Loads," IEEE/RSJ International Conference on Intelligent Robots and Systems (IROS), Taipei, Taiwan, October 18–22, pp. 2325–2332.
[13] Rucker, D. C., Jones, B. A., and Webster, R. J., III, 2010, "A Geometrically Exact Model for Externally Loaded Concentric-Tube Continuum Robots," IEEE Trans. Rob., **26**(5), pp. 769–780.
[14] Zheng, T., Branson, D. T., Guglielmino, E., Kang, R., Medrano-Cerda, G. A., Cianchetti, M., Follador, M., Godage, I. S., and Caldwell, D. G., 2013, "Model Validation of an Octopus Inspired Continuum Robotic Arm for Use in Underwater Environments," ASME J. Mech. Rob., **5**(2), p. 021004.
[15] Webster, R. J., III, and Jones, B. A., 2010, "Design and Kinematic Modeling of Constant Curvature Continuum Robots: A Review," Int. J. Rob. Res., **29**(13), pp. 1661–1683.
[16] Chirikjian, G. S., and Burdick, J. W., 1994, "A Modal Approach to Hyper-Redundant Manipulator Kinematics," IEEE Trans. Rob. Autom., **10**(3), pp. 343–354.
[17] Tatlicioglu, E., Walker, I. D., and Dawson, D. M., 2007, "Dynamic Modelling for Planar Extensible Continuum Robot Manipulators," IEEE International Conference on Robotics and Automation, Rome, Italy, April 10–14, pp. 1357–1362.
[18] Jones, B. A., Gray, R. L., and Turlapati, K., 2009, "Three Dimensional Statics for Continuum Robotics," IEEE/RSJ International Conference on Intelligent Robotics and Systems (IROS 2009), St. Louis, MO, October 10–15, pp. 2659–2664.
[19] Renda, F., Cianchetti, M., Giorelli, M., Arienti, A., and Laschi, C., 2012, "A 3D Steady-State Model of a Tendon-Driven Continuum Soft Manipulator Inspired by the Octopus Arm," Bioinspiration Biomimetics, **7**(2), p. 025006.
[20] Rucker, D. C., Webster, R. J., III, Chirikjian, G. S., and Cowan, N. J., 2010, "Equilibrium Conformations of Concentric-Tube Continuum Robots," Int. J. Rob. Res., **29**(10), pp. 1263–1280.
[21] Rucker, D. C., and Webster, R. J., III, 2011, "Statics and Dynamics of Continuum Robots With General Tendon Routing and External Loading," IEEE Trans. Robot., **27**(6), pp. 1033–1044.
[22] Spillmann, J., and Teschner, M., 2007, "CORDE: Cosserat Rod Elements for the Dynamic Simulation of One-Dimensional Elastic Objects," Eurographics/ACM SIGGRAPH Symposium on Computer Animation, San Diego, CA, August 3–4, pp. 63–72.
[23] Lang, H., Linn, J., and Arnold, M., 2010, "Multi-Body Dynamics Simulation of Geometrically Exact Cosserat Rods," Multibody Syst. Dyn., **25**(3), pp. 285–312.
[24] Chirikjian, G. S., 1995, "Hyper-Redundant Manipulator Dynamics: A Continuum Approximation," Adv. Rob., **9**(3), pp. 217–243.
[25] Gravagne, I. A., Rahn, C. D., and Walker, I. D., 2003, "Large Deflection Dynamics and Control for Planar Continuum Robots," IEEE/ASME Trans. Mechatronics, **8**(2), pp. 299–307.
[26] Rone, W. S., and Ben-Tzvi, P., 2012, "Continuum Manipulator Statics Based on the Principle of Virtual Work," ASME Paper No. IMECE2012-87675.
[27] Rone, W. S., and Ben-Tzvi, P., 2013, "Continuum Robot Dynamics Utilizing the Principle of Virtual Power," IEEE Trans. Rob., **30**(1), pp. 275–287.
[28] Xu, K., and Simaan, N., 2010, "Analytic Formulation for Kinematics, Statics, and Shape Restoration of Multibackbone Continuum Robots Via Elliptic Integrals," ASME J. Mech. Rob., **2**(1), p. 011006.
[29] Jung, J., Penning, R. S., Ferrier, N. J., and Zinn, M. R., 2011, "A Modeling Approach for Continuum Robotic Manipulators: Effects of Nonlinear Internal Device Friction," IEEE/RSJ International Conference on Intelligent Robots and Systems (IROS), San Francisco, CA, September 25–30, pp. 5139–5146.
[30] Giri, N., and Walker, I. D., 2011, "Three Module Lumped Element Model of a Continuum Arm Section," IEEE/RSJ International Conference on Intelligent Robots and Systems (IROS), San Francisco, CA, September 25–30, pp. 4060–4065.
[31] Kane, T. R., and Levinson, D. A., 1983, "The Use of Kane's Dynamical Equations in Robotics," Int. J. Rob. Res., **2**(3), pp. 3–21.
[32] Haghshenas-Jaryani, M., and Vossoughi, G., 2009, "Modeling and Sliding Mode Control of a Snake-Like Robot With Holonomic Constraints," IEEE International Conference on Robotics and Biomimetics (ROBIO 2008), Bangkok, Thailand, February 22–25, pp. 454–461.
[33] Vossoughi, G., Pendar, H., Heidari, Z., and Mohammadi, S., 2007, "Assisted Passive Snake-Like Robots: Conception and Dynamic Modeling Using Gibbs–Appell Method," Robotica, **26**(3), pp. 267–276.
[34] Zhuang, W., Liu, X., Fang, C., and Sun, H., 2008, "Dynamic Modeling of a Spherical Robot With Arms by Using Kane's Method," 4th International Conference on Natural Computation (ICNC '08), Jinan, Shandong, China, October 18–20, pp. 373–377.